Anodized aluminum surface with topography-mediated antibacterial properties

Henry Agbe, Dilip Kumar Sarkar*, X.-Grant Chen,

Department of Applied Science, Aluminum Research Center – REGAL, University of Québec at Chicoutimi, Chicoutimi, QC, Canada, G7H 2B1.

KEYWORDS: anodized aluminum; biomimicry; topography-mediated antibacterial surfaces; nosocomial infections.

ABSTRACT:

Topography-mediated antibacterial surfaces that inactivate bacteria by physical contact are gaining attention in recent times. Contrary to conventional antibacterial coatings, topography-mediated antibacterial surfaces do not suffer from coating instability and possible toxicity problems. In this study, a one-step hard anodization process has been deployed to fabricate a topography-mediated antibacterial aluminum surface. By optimizing anodization parameters, such as concentration of electrolyte, current density and anodization time, desirable features of micro-nanoscale morphology were achieved. The optimum condition of anodized aluminum that provided pores of diameter of 151 ± 37 nm effectively killed 100% E. coli bacteria.

Introduction

Many organisms such as cicada, dragonfly and damselfly use their micro-nanoscale surface structures to adapt, fight colonization or as evolutionary surviving strategy[1]. These micro-nanostructures on the wings of most insects and plant parts such as lotus leaves are composed of natural long chain palmitic (hexadecanoic**)** and stearic (octadecanoic) fatty acids[2], rendering them superhydrophobic. Superhydrophobic surfaces are known to exhibit water contact angle (WCA) > 150° and a tilting angle < 10°[3]. Due to their ability to inhibit initial bacterial attachment and subsequent biofilm formation, superhydrophobic coatings are considered important strategy for designing anti-biofouling surfaces[3]. However, they lose their water roll-off property over time due to coating instability[4]. Hence, novel antibacterial strategies that kill bacteria on contact via surface topography have become an area of intense scientific focus in recent times[1, 5-7]. These novel antibacterial strategies herein referred as topography-mediated antibacterial surfaces exhibit antibacterial property by inducing mechanical stresses to damage cell membrane, leading to bacterial cell death[6, 8-9].

Since topography-mediated antibacterial cicada wings was first reported by Ivanova and co-workers[5] against *Pseudomonas aeruginosa* (PA) (gram -ve) bacterium and their subsequent report on synthetic analogue, black silicon[10], various artificial antibacterial surfaces mediated by micro-nanoscale patterns, such as nanocones, nanofibers and nanopillars, have been fabricated on metals, ceramics and polymers[11-13]. These approaches provide a paradigm shift in fabrication of the next generation novel antibacterial surfaces. Contrary to conventional antibacterial coatings, such as leachable antibacterial agents (metallic silver and copper), these do not suffer from coating instability, possible toxicity and antibacterial resistance problems[6]. Thus, they are more eco-

sustainable and have great potential for medical implant prostheses, and frequently touched surface applications. In particular, these could be useful as antibacterial touched surfaces, in support of existing hand hygiene, masking and social distancing protocols aimed at curbing both community and healthcare spread of the *severe acute respiratory syndrome coronavirus 2* (SARS-CoV-2) infections. Surfaces in frequently touched areas can actually become potential reservoir for transmission of various pathogens making them serious infection prone health risk. For example, SARS-CoV-2, methicillin-resistant *Staphylococcus aureus* (MRSA), *Escherichia coli* (E. coli), *Pseudomonas aeruginosa* (PA) and *Clostridium difficile* spores can survive on inanimate environmental surfaces for days, weeks and months[14-16]. Thus, commonly touched inanimate environmental surfaces such as elevator buttons, doorknobs, handrails, faucet handles, light switches and medical equipment should be rendered antibacterial to limit the spread of pathogenic infections.

Aluminum is a very attractive material for engineering constructions and many aluminum components are widely used in medical devices[17] and in frequently touched surfaces[18]. Aluminum can be transformed into antibacterial surface via low cost wet chemistry process. Surprisingly, only few studies have been reported on antibacterial aluminum prepared by wet chemistry[17-19]. Hasan et al.[19] recently reported antiviral aluminum surfaces fabricated using a chemical etching process, which were effective against the current SARS-CoV-2. In a related study[18], previously, they demonstrated the antimicrobial activity of a topography-mediated aluminum, fabricated by chemical etching against common multi-drug resistant (MDR) pathogens such as *Pseudomonas aeruginosa* (P.A) and *Staphylococcus aureus (*S.A), and on respiratory viruses such as *respiratory syncytial virus* (RSV) and *rhino virus* (RV). While desirable nanoscale topography are achievable

by chemical etching, mechanical property of nanoscale features are rather weak[20]. An alternative surface treatment process resulting in aluminum surfaces with excellent anti-corrosive, tribological and mechanical properties such as anodization appears promising in terms of robustness[21].

Considering the need for the microstructural stability with better mechanical properties for a long-term service life and protection, we report herein a novel topography-mediated antibacterial aluminum surfaces, fabricated via anodization. In this study, parameters of anodization such as concentration of electrolyte, current density and anodization time have been systematically varied for obtaining optimal topography that showed the best antibacterial performance. The results of the optimization process and the antibacterial properties have been demonstrated. It has been shown that the excellent antibacterial performance was purely driven by the surface topography of the anodized aluminum.

MATERIALS AND METHODS

Pre-treatment of aluminum: AA6061-T6 aluminum sheets of dimensions 1″ × 2″ were ultrasonically degreased (Branson® Ultrasonic Bath, 230 Vac, 50 Hz) in a diluted soap solution for 15 minutes. The cleaned Al substrates were immersed in 1 M NaOH (VWR) etchant for 3 minutes at 55 °C to remove a superficial oxide layer. Subsequently, etched Al substrates were immersed in HNO_3 solution (10 wt. %, VWR) for desmutting, followed by further rinsing thoroughly in distilled water. Finally, etched Al substrates were dried at 70 ˚C in an oven overnight.

Anodizing in acid electrolytes: Etched and as-received AA6061-T6 aluminum sheets used as anode and cathode, respectively, were immersed in 3 wt.%, 15 wt.% and 45 wt.% concentrations

of H_3PO_4 acidic electrolyte (VWR). The anodization process was performed by optimizing current density from 7 to 40 mA/cm^2 and from 30 to 120 minutes using a galvanostatic 600 W direct current power system (Ametek Sorensen DCS 100-12E, Chicoutimi, QC, Canada). To ensure uniform heat distribution and prevent burning, the electrochemical cell was equipped with a cold water circulating coolant bath (5 °C) and a Teflon stirring magnetic unit, rotating at 2000 rpm throughout the anodization process. During anodization, the two electrodes were separated in parallel by a distance of 1.5 cm. Anodized aluminum coupons were finally sonicated for 30 minutes in distilled water to remove residual electrolytes, followed by drying at 70 ˚C in an electric oven (VWR) overnight. For quality control and reproducibility, each experiment was repeated in triplicate.

Sample characterization: The surface morphological and elemental analyses of anodized aluminum coupons were performed using scanning electron microscopy (SEM, JEOL JSM-6480 LV) equipped with energy dispersive X-ray spectroscopy (EDS). High-resolution SEM micrographs were analyzed in a Java-based image-processing program - Image J (http://rsbweb.nih.gov/ij/), to determine the morphological features. A minimum of 30 different SEM micrographs were taken from each coupon for analysis. Approximately 1,000 independent measurements were analyzed. Prior to SEM analysis, anodized aluminum coupons were metalized with gold coating (~8 nm) using an Edwards Scancoat Six Sputter Coater. The surface roughness of anodized aluminum was studied using an optical profilometry (MicroXAM-100 HR 3D surface profilometer, *NANOVEA*, Irvine, USA).

Antibacterial study by a novel dry seeding assay: *Escherichia coli* bacterium strain (ATCC 8739) was grown overnight from frozen (−80 °C) glycerol stock in tryptic soy broth (TSB) (Hardy Diagnostics) at 37 °C, and then passaged on fresh TSB (37 °C) to obtain bacterial cell density of 10^8 colony forming units/milliliter (CFU)/mL. Bacterial cell density was adjusted to OD_{625} = 0.1. To mimic near dry conditions of frequently touched surfaces in hospital setting, we have developed a facile "dry seeding" approach to study the bactericidal activity of anodized aluminum coupons. Briefly, 5 μL of *Escherichia coli* inoculum (1.5×10^8) was seeded on a sterile 1″ × 1″ area of anodized aluminum and as-received aluminum coupons (as control). Next, coupons were incubated at ambient conditions of 25 °C and 50 ± 10% relative humidity in a cell culture plates for pre-determined contact time (1, 3 and 4 h). Subsequently, bacterial cells were sampled with sterile swab from coupons into physiological saline (0.85 wt.% NaCl) followed by serial dilutions and plating on tryptic soy agar (TSA) to obtain a bacterial lawn. Plates were finally incubated at 37 °C for 24 h to yield countable viable bacterial colonies (30–300 colonies per plate). For continuous bacterial loading study, same procedure was followed except that quantitative recovery was done after 24, 48, 72 and 96 h. These anodized aluminum coupons were inoculated 1, 2, 3 and 4 times, respectively. Positive controls were also performed for t = 0 and t = 4 h to ascertain bacterial cell viability. Three independent experiments were performed in duplicate to determine the number of viable bacteria. Antibacterial efficiency was calculated from [(A-B)/A] ×100 %. Where A = CFU/cm^2 of viable bacteria on anodized aluminum coupon and B = CFU/cm^2 of viable bacteria on as-received aluminum coupon (as control). Data were analyzed by one-ANOVA (analysis of variance) with Tukey–Kramer multiple comparison test. Data were considered statistically significant for $p < 0.05$.

RESULTS AND DISCUSSIONS

Figure 1(A) and (B) show the potential-time (E-T) transient curve for the anodization process. As typical for galvanostatic anodization, potential increases sharply at the initial stage and reduces gradually with steady state oxide growth and dissolution over anodization time[22]. The sharp increase in potential is due to high resistance imposed by the compact barrier oxide layer. It should be mentioned that barrier oxide results from egressing Al^{+} ion (from the metal/oxide interface) and ingress O^{2-} ion (from the oxide/metal interface), following local electrolytic water splitting[23]. As the anodization continues, potential increases linearly with time until it reaches a local maximum called the breakdown potential.

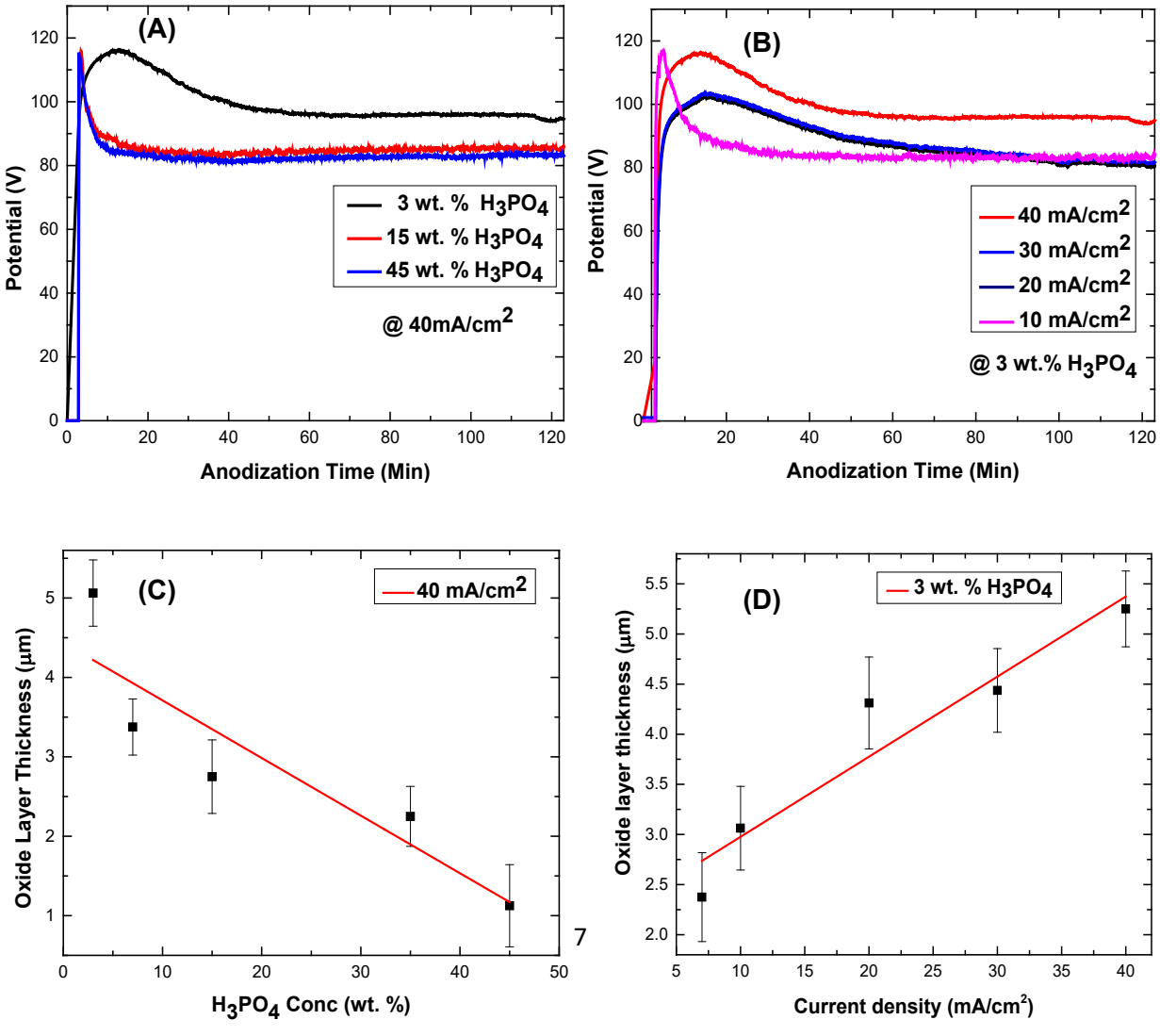

Figure 1. Parameters of anodization process: (A) Voltage-time (V-t) transient curve as a function of concentration of H_3PO_4 acid; (B) Voltage-time (V-t) transient curve as a function of current density; (C) Thickness of anodized alumina oxide layer as a function of concentration of H_3PO_4 acid and (D) Thickness of anodized alumina oxide layer as a function of current density.

Beyond the breakdown potential, it decreases gradually until it reaches a steady state-forming potential[22]. For a 3 wt.% H_3PO_4, a steady state-forming potential of 96 V was attained after 60 minutes. Beyond this, the potential remains constant for an equilibrium oxide layer growth and dissolution, which leads to a complete formation of porous oxide after 120 minutes. Similar trend was observed for the other H_3PO_4 concentrations such as 15 and 45 wt.%. For example, a steady state-forming potential of 82 V was attained for 45 wt.% H_3PO_4 after 50 minutes, which led to complete anodization after 120 minutes. Notably, steady state-forming potential decreased with increasing H_3PO_4 concentration. This may be due to the inverse relation between steady state-forming potential and acid concentration, which is commonly explained by the oxygen bubble growth model[24]. According to this model, total anodizing current (J_{Total}) contributing to oxide layer growth and dissolution consists of both ionic current (J_{ion}) and electronic current (J_e) as shown in Equation 1[25]:

$$J_{Total} = J_{ion} + J_e \quad (1)$$

where J_{Total} is the total current, J_{ion} the ionic current, and J_e the electronic current. The ionic current contributing to migration of anions and cations at the anode can be expressed as Equation 2.

$$2Al^{3+} + 3O^{2-} \rightarrow Al_2O_3 \quad (2)$$

similarly, the electronic current leading to oxygen evolution at the anode can be expressed as Equation 3.

$$4O^{2-} \rightarrow 2O_2 \uparrow + 8e \quad (3)$$

However, since ionic current dominates at the initial stage of anodization, the required net current for overcoming the resistance of the compact barrier oxide layer is induced by ionic current[25]. Contrarily, beyond the breakdown potential, electronic current increases at the expense of ionic current, resulting in a decrease in total current J_{ion} and potential, with oxygen evolution and a lower porous oxide growth[24-25]. Hence, high acid concentration such as 45 wt.% H_3PO_4 resulted in a lower steady state-forming potential of 82 V. On the other hand, a low acid concentration such as 3 wt.% H_3PO_4 led to higher steady state-forming potential of 96 V. A similar observation was made by Zhang et al.[24] on anodized Titanium alloy using NH_4F acid as electrolyte. They demonstrated that NH_4F concentration of 0.5 wt.% resulted in a low steady state-forming potential of 55 V compared to 0.1 wt.% NH_4F acid with a high steady state-forming potential of 95 V. As shown in Figure 1(B), steady state-forming potential increased with increasing current density. As a result, a steady state-forming potential of 96 V was achieved for 40 mA/cm^2, compared to 78 V for 10 mA/cm^2. In addition, increasing acid concentration resulted in decreasing oxide layer thickness. Thus, a porous oxide thickness of 1.1 ± 0.5 μm was obtained for 45 wt.% H_3PO_4 concentration, as opposed to a thickness of 5.3 ± 0.4 μm for 3 wt.% H_3PO_4 (Figure 1(C)). Contrarily, current density increased linearly with oxide layer thickness. Consequently, 10

mA/cm^2 led to an oxide layer thickness of 3.1 ± 0.4 µm. On the other hand, 40 mA/cm^2 resulted in a thickness of 5.3 ± 0.4 µm (Figure 1(D)).

Since topographical features such as pore diameter, cell diameter or pitch, oxide thickness and roughness are important for antibacterial activity[6], topographical features were analyzed using Equations 4, 5 and 6[22].

$$n = \frac{10^{14}}{P_h} = \frac{2.10^{14}}{\sqrt{3} * D_c^2} \quad (4)$$

$$W = \frac{Dc - Dp}{2} \quad (5)$$

$$\alpha = \frac{\pi}{2\sqrt{3}} \left(\frac{D_p}{D_c}\right)^2 = 0.907 \left(\frac{D_p}{D_c}\right)^2 \quad (6)$$

where η is the pore density, P_h is the surface area of a single hexagonal cell, D_p is the pore diameter and D_c is the cell diameter in nm. Generally, phosphoric acid with low acid concentration, such as 3% H_3PO_4 and a high current density such as 40 mA/cm^2, led to a large pore diameter, a large cell diameter, a high surface roughness and efficient bactericidal property, compared to 45 wt.% H_3PO_4 at a low current density such as 10 mA/cm^2. The low acid concentration leading to increased potential and larger morphological features can be explained by oxygen bubble growth model[25]. By contrast, the classical field-assisted growth model explains the reason for increased current density, resulting in larger morphological features. Thus, 3 wt.% H_3PO_4 (herein referred as 3HP40), exhibited a pore diameter of 151 ± 37 nm, a cell diameter of 239 ± 53 nm, a roughness (rms) of 2.9 ± 0.7 µm and bactericidal efficiency of 100%. Contrarily, 45 wt.% H_3PO_4 (herein referred as 45HP40) showed a low pore diameter of 55 ± 12 nm, a cell diameter of 115 ± 16 nm, a roughness (rms) of 0.8 ± 0.1 µm and a bactericidal efficiency of 85% (details can be found in Supplementary data, Figure S1 and Table S1).

Antibacterial Activity

Antibacterial activity was studied by a novel dry seeding assay against E. coli bacterium on anodized aluminum coupons. The objective here was to mimic a real-world scenario. Thus, we inoculated test coupons with E. coli inoculum at ambient conditions of 25 °C and relative humidity of 50 ± 10% in a cell culture plate for pre-determined contact time of 1-4 h. Figure 2 shows the effects of morphological features on E. coli bacterial killing. Generally, antibacterial efficiency of anodized aluminum coupon increased linearly with increased pore diameter, cell diameter, oxide layer thickness and root mean square roughness. In combination with Figure 1, the results show that anodized aluminum coupon having a lower H_3PO_4 concentration such as 3 wt.% and a higher current density such as 40 mA/cm^2, exhibited a high antibacterial efficiency compared to anodized aluminum coupon with a higher H_3PO_4 concentration such as 45 wt.%.

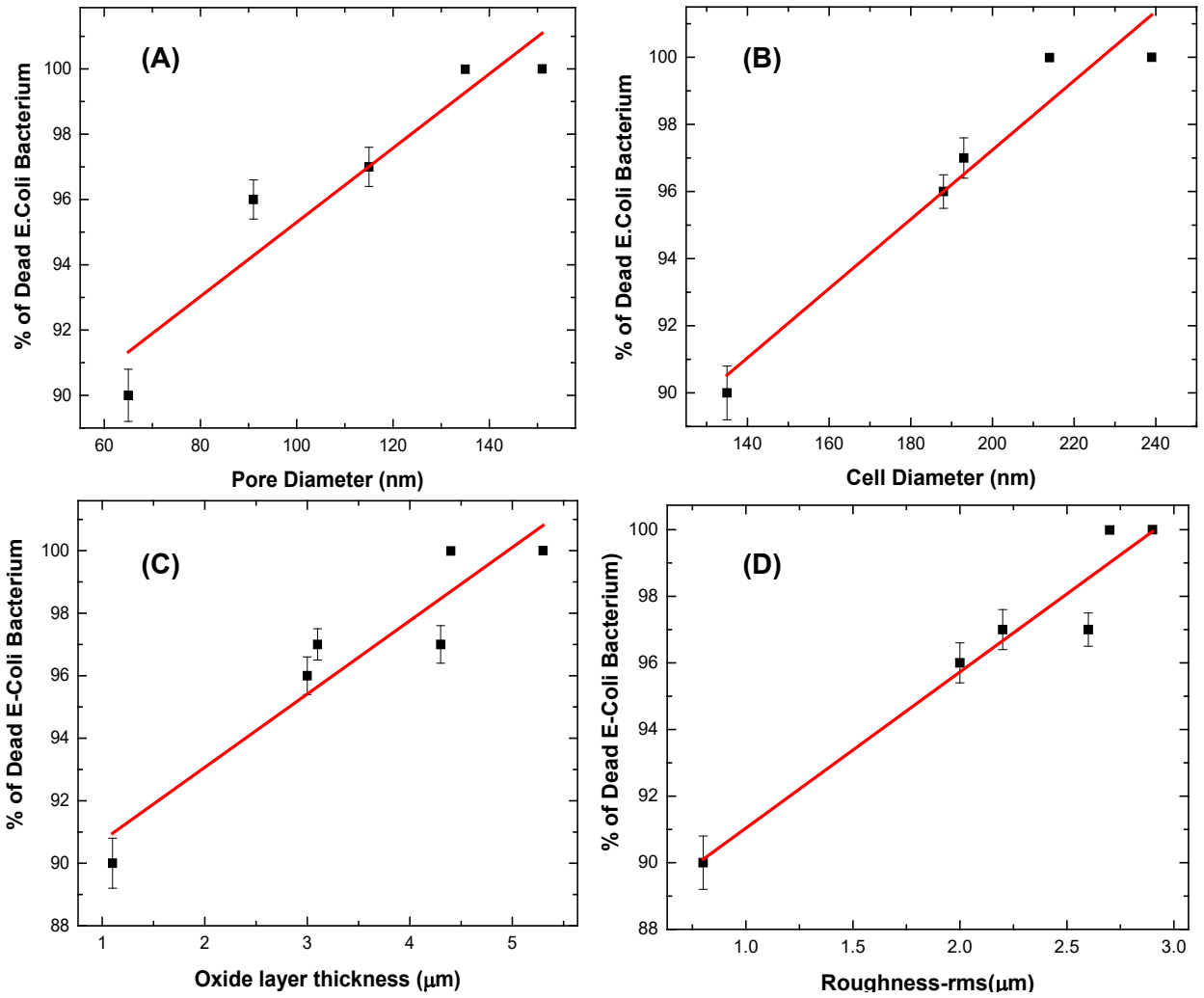

Figure 2. Effects of morphological features resulted from different anodization parameters on E. coli bacteria killing efficiency: (A) pore diameter, (B) cell diameter, (C) oxide thickness, (D) surface roughness (rms).

In particular, for 3 wt.% H_3PO_4, increasing the current density from 10 mA/cm^2 to 40 mA/cm^2 led to increase in both pore and cell diameters with a corresponding increase in bactericidal performance (Details can be found in Supplementary data, Table S1 and Figures S1 and S2). For instance, the pore diameter increased from 65 ± 15 μm to 151 ± 37 μm for respective current

densities of 7 to 40 mA/cm^2,corresponding an increase of antibacterial activity from 90 to 100% (Figure 2(A)). Similarly, the cell diameter or pitch increased from 135 ± 10 μm to 239 ± 53 μm for same current densities with a corresponding increase in antibacterial activity from 90 to 100%, respectively (Figure 2(B)). As would be expected, the current density also increased linearly with porous oxide thickness and hence antibacterial activity. Oxide thickness of 1.1 ± 0.5 μm and 5.3 ± 0.4 μm, were obtained for current densities of 7 and 40 mA/cm^2, respectively, resulting in 90% and 100% antibacterial efficiency respectively, (Figure 2(C)). Similar trend was observed for the surface roughness and bacterial efficiency (Figure 2(D)). It should be mentioned that exact antibacterial mechanism for 3 wt.% H_3PO_4 anodized aluminum coupon-3HP40, was not fully elucidated here. Bacterial attachment on both biotic and abiotic substratum surfaces is a complex phenomenon, involving surface chemistry and substratum surface morphology, bacterial cell type and adhesion, Van der Waals interactions, extra polymeric substance (EPS) and quorum sensing molecules[26]-[27]. However, we hypothesize that the micro-nanoscale topography features, characterized as pore diameter, cell diameter (pitch) and roughness (rms) may be responsible for the excellent bactericidal activity. It should be mentioned that previous reports have confirmed a topography-mediated antibacterial surface[5]. In fact, Ivanova et al.[5] first reported on topography-mediated bactericidal effects on *Psaltoda claripennis* cicada wings. In their work, they demonstrated that by pure physical contact of *Pseudomonas aeruginosa* (PA) (gram -ve) bacterium on micro-nanoscale patterns cicada wings, PA died in 30 minutes. These nanoscale pillar arrays were hexagonal and conical shapes, with spherical caps of diameter ~ 60 nm, pitch of 170 nm and height of 200 nm[5]. Also, Kelleher et al.[9] showed that nano-pillar array of diameters ranging from 156 ± 29 nm to 207 ± 62 nm and pitch ranging from 165 ± 8 nm to 251 ± 31 nm, could effectively kill Pseudomonas fluorescens bacterium. However, direct comparison of reported results in the

literature must be treated with caution as the difference may arise due to different experimental conditions. In the present report, 3 wt.% H_3PO_4 anodized aluminum coupon-3HP40 was compared with the control coupons of as-received aluminum and of antibacterial solid copper (C11000 of 99.9% Cu) in a novel dry seeding assay. It is worthy to note that since 2008, copper has been registered by the United States Environmental Protection Agency (US-EPA) as an antimicrobial touched surface, and regarded as gold standard for comparing other non-porous antimicrobial touched surfaces [28-30]. Also note that existing protocols such as the ASTM E2180[31], the Japanese Standard JIS Z2801[32] or the ISO 22196[33] stipulate conditions of high liquid medium humidity > 90% and temperature of 35 ± 1 °. While these protocols might be ideal for biomedical implant applications, they do not reflect the near dry conditions of inanimate environmental surfaces in close proximity to patients, typified by a comfortable humidity and temperature[34]. Thus, these protocols may not truly predict the efficacy of antibacterial surfaces under realistic conditions[34].

Figure 3 shows representative images of E. coli bacterium colonies on 3HP40 test coupon, relative to the control coupons. Compared to anodize aluminum coupon-H3P40, as-received aluminum displayed a confluent bacterial growth with evenly spread colonies on TSA media even after 4 h E. coli bacterium contact. On the contrary, it is noticeable that 3 wt.% H_3PO_4 anodized aluminum coupon-3HP40 killed virtually all bacteria under 1 h of E. coli bacterium contact. The number of colonies on as-received aluminum at time 0 h, 1 h, and 4 h were 4.5×10^7, 4.207×10^7 and 2.24×10^7, respectively. These represent a 6.6% or 0-log reduction, 39% or 0.2 log reduction and 51% or 0.3 log reduction, respectively (see Table S3 of supplementary data). In contrast, the 3 wt.% H_3PO_4 anodized aluminum coupon-3HP40 achieved a bactericidal efficiency of 99.99998% or 6.5 log reduction after 1 h of contact.

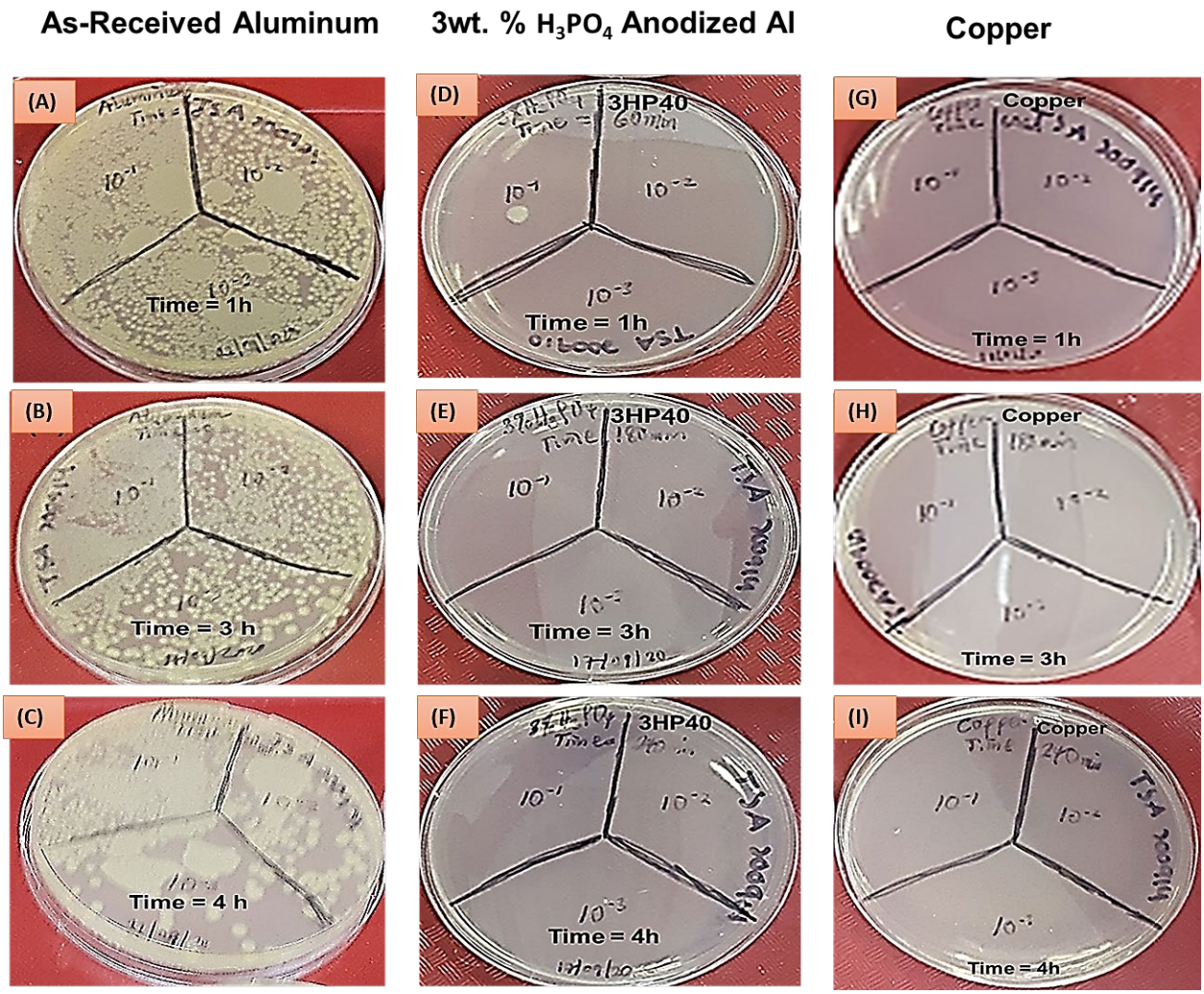

Figure 3. Representative images of colonies of E. coli in contact with: as-received aluminum coupon from 1- 4 h (A)-(C); 3 wt.% H_3PO_4 anodized aluminum coupon-3HP40 from 1- 4 h (D)-(F); and copper coupon from 1- 4 h (G)-(I).

The results of 3 wt.% H_3PO_4 anodized aluminum are very comparable with the commercially available antimicrobial copper, of which both exhibited a 100% bactericidal efficiency after 1 h under same conditions (Figure 4). It has to be noted that minimum microbiologic bacterial loads

acceptable in hospital inanimate environmental surfaces is 2.5 cfu/cm^2 Thus, bacterial colonies of 2.24 × 10^7 on as-received aluminum could be regarded worrisome; since such surface contamination could be a potential reservoir for spread of nosocomial infection.

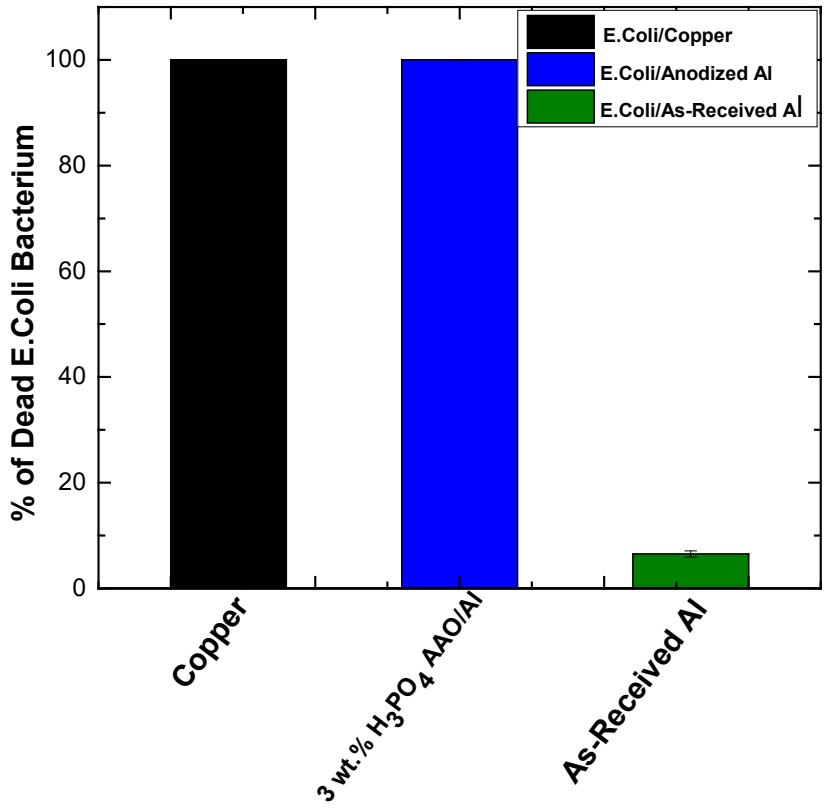

Figure 4. Bactericidal efficiency of E. coli bacteria on 3 wt.% H_3PO_4 anodized aluminum coupon-3HP40 compared to control samples (as-received aluminum and copper) under 1 h of contact. Data represent three independent experiments

According to the US-EPA, touched surfaces with the claim of antibacterial property ought to kill or inhibit the growth of bacteria to a minimum of 3-log reduction or 99.9 %[35]. Thus, the aforementioned 3 wt.% H_3PO_4 anodized aluminum is very promising and shows great potentials as the ideal condition for practical antibacterial touched surface applications. Figure 5(A) and

(B) show the SEM micrographs of as-received aluminum and 3 wt.% H_3PO_4 anodized aluminum coupon-3HP40, respectively. Notably, rod shaped E. coli bacteria (green arrows) are clearly seen on as-received aluminum (Figure 5(A).

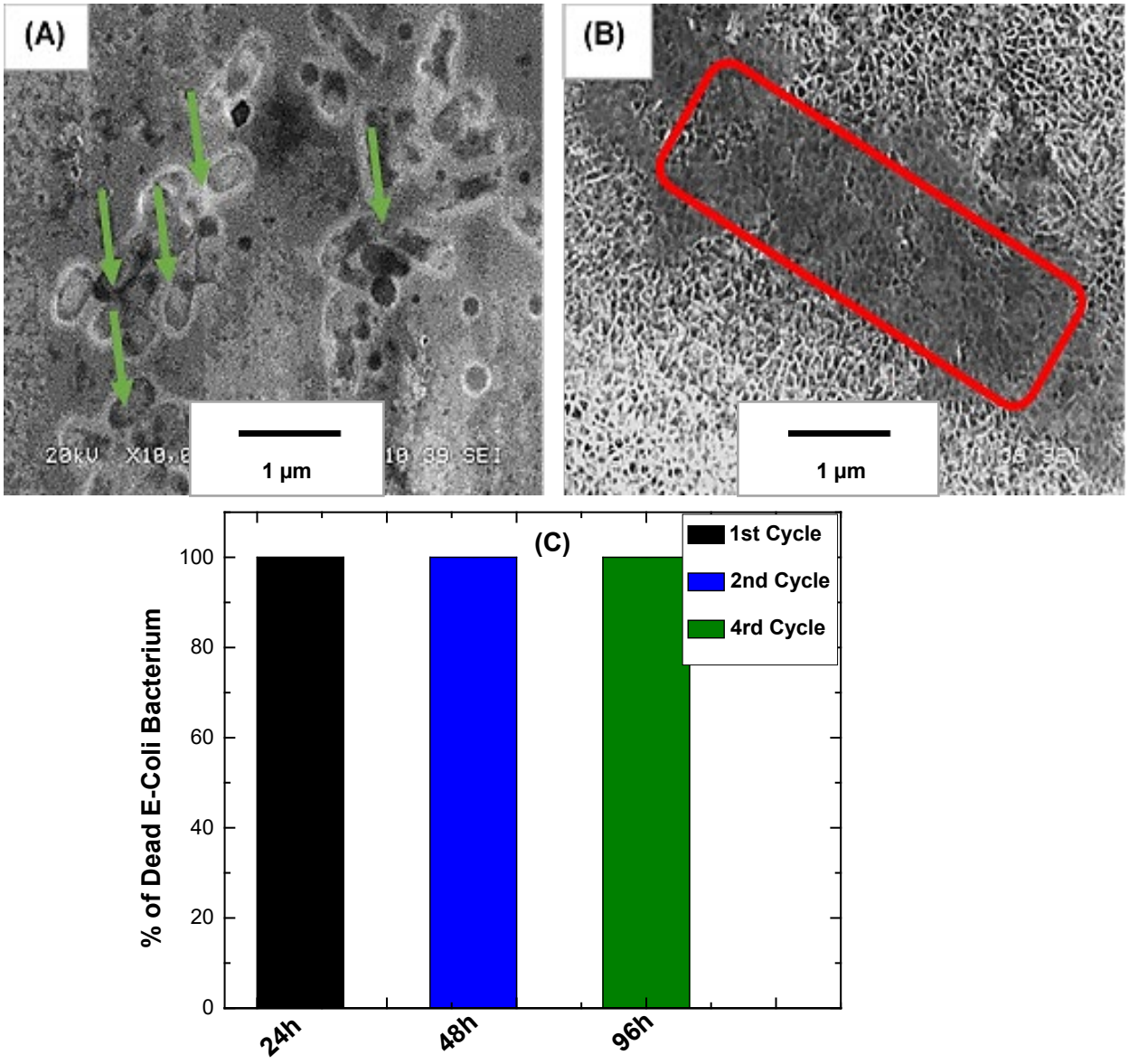

Figure 5. Representative SEM microimages of colonies E-Coli bacteria on: (A) as-received aluminum coupon; (B) on 3 wt.% H_3PO_4 anodized aluminum coupon-

3HP40; and (C) a graphical representation of 96 h E. coli bacteria continuous loading on 3 wt.% H_3PO_4 anodized aluminum coupon-3HP40. The green arrows in (A) show live E. coli bacteria and the region in red in (B) indicates dead E. coli bacteria, respectively. Data represent three independent experiments.

In contrast, live E. coli bacteria cells are not seen on 3 wt.% H_3PO_4 anodized aluminum coupon-3HP40, except for cytoplasmic material (shown in the region in red) (Figure 5(B)), which leaked out from bacteria after they were deformed and sunk into the nanopores[8]. In fact, the antibacterial mechanism for topography-mediated antibacterial surfaces such as cicada wings has been attributed to the self-induced shear stresses on bacterial cell membrane in contact with nano-pillars [1, 5, 36-37]. Specifically, higher surface roughness, coupled with micro-nanoscale patterns increases surface area for attachment from multiple focal points and overall bacterial-substratum interaction. A stronger bacterial-substratum interaction would presumably enhance the tendency for bacterial membrane to be stretched out, leading to an irreversible rupture and death[32]. However, in the present work, a micro-nanoscale pattern was achieved by nano-pore arrays, different from other nanostructures such as nanopillars reported previously[5-7]. Thus, we hypothesize that upon bacterial attachment on the surface of the anodized aluminum (3HP40), E. coli bacteria become suspended under gravity within nano-pore arrays of anodized surface, where the suspended regions of anodized pores induce shear stresses on E. coli cell membrane. In their attempt to avoid uncomfortable suspended regions, E. coli bacteria release extra polymeric substance (EPS), which further enhance bacterial attachment on nano-pores of anodized aluminum surface (3HP40). Consequently, this leads to membrane deformation, cytoplasmic material leakage, failure of cell membrane integrity[8] and bacterial death. Figure 5(C) shows a

graphical representation of a 96 h continuous E. coli bacterial loading study on the 3 wt.% H_3PO_4 anodized aluminum coupon-3HP40. The samples were monitored at 24 h interval within cycles to evaluate the long-term activity of the anodized aluminum surface. Interestingly, even after 96 h E. coli bacteria continuous loading cycles, the 3 wt.% H_3PO_4 anodized aluminum coupon-3HP40 was still bioactive with a 100% bactericidal efficiency. Thus, this anodized aluminum surface with excellent bactericidal efficiency and durability looks promising for antibacterial touched surface applications and an adjunct to hand hygiene for reducing potential bacterial infections in hygiene critical environments.

CONCLUSIONS

In the present study, a topography-mediated novel antibacterial aluminum surface was fabricated using a one-step hard anodization process. Anodization parameters such as electrolyte concentration, time and current density were optimized. 3wt.% H_3PO_4 anodized aluminum at current density of 40 mA/cm^2 and anodization time of 120 minutes exhibited a larger pore diameter (151 ± 37 nm), larger cell dimeter (239 ± 53 nm), higher oxide layer thickness (5.3 ± 0.4 nm) and higher *rms* roughness (2.9 ± 0.7μm), compared to 45 wt.% H_3PO_4 anodized aluminum at same conditions. Furthermore, 3wt.% H_3PO_4 anodized aluminum at current density of 40 mA/cm^2 compared favourably with antibacterial solid copper with 100% bactericidal efficiency after 1 h E. coli bacterium contact. Overall, the fabrication of topography-mediated antibacterial aluminum presents a novel approach to be considered for the use of the next generation frequently touched surfaces.

Acknowledgement

We acknowledge the financial support from Fonds de recherche du Québec - Nature et technologies (FRQNT) under the grant number 2018-LU-210883.

References

1. Hasan, J.; Roy, A.; Chatterjee, K.; Yarlagadda, P. K., Mimicking insect wings: The roadmap to bioinspiration. *ACS Biomaterials Science & Engineering* **2019,** *5* (7), 3139-3160.
2. Ivanova, E. P.; Nguyen, S. H.; Webb, H. K.; Hasan, J.; Truong, V. K.; Lamb, R. N.; Duan, X.; Tobin, M. J.; Mahon, P. J.; Crawford, R. J., Molecular organization of the nanoscale surface structures of the dragonfly Hemianax papuensis wing epicuticle. *PLoS One* **2013,** *8* (7), e67893.
3. Crawford, R. J.; Ivanova, E. P., *Superhydrophobic surfaces*. Elsevier: 2015.
4. Agbe, H.; Sarkar, D. K.; Chen, X.-G.; Faucheux, N.; Soucy, G.; Bernier, J.-L., Silver–Polymethylhydrosiloxane Nanocomposite Coating on Anodized Aluminum with Superhydrophobic and Antibacterial Properties. *ACS Applied Bio Materials* **2020,** *3* (7), 4062-4073.
5. Hasan, J.; Webb, H. K.; Truong, V. K.; Pogodin, S.; Baulin, V. A.; Watson, G. S.; Watson, J. A.; Crawford, R. J.; Ivanova, E. P., Selective bactericidal activity of nanopatterned superhydrophobic cicada Psaltoda claripennis wing surfaces. *Applied microbiology and biotechnology* **2013,** *97* (20), 9257-9262.
6. Ivanova, E. P.; Hasan, J.; Webb, H. K.; Truong, V. K.; Watson, G. S.; Watson, J. A.; Baulin, V. A.; Pogodin, S.; Wang, J. Y.; Tobin, M. J., Natural bactericidal surfaces: mechanical rupture of Pseudomonas aeruginosa cells by cicada wings. *Small* **2012,** *8* (16), 2489-2494.
7. Ivanova, E. P.; Linklater, D. P.; Werner, M.; Baulin, V. A.; Xu, X.; Vrancken, N.; Rubanov, S.; Hanssen, E.; Wandiyanto, J.; Truong, V. K., The multi-faceted mechano-bactericidal mechanism of nanostructured surfaces. *Proceedings of the National Academy of Sciences* **2020,** *117* (23), 12598-12605.
8. Bandara, C. D.; Singh, S.; Afara, I. O.; Wolff, A.; Tesfamichael, T.; Ostrikov, K.; Oloyede, A., Bactericidal effects of natural nanotopography of dragonfly wing on Escherichia coli. *ACS applied materials & interfaces* **2017,** *9* (8), 6746-6760.
9. Kelleher, S. M.; Habimana, O.; Lawler, J.; O'reilly, B.; Daniels, S.; Casey, E.; Cowley, A., Cicada wing surface topography: an investigation into the bactericidal properties of nanostructural features. *ACS applied materials & interfaces* **2016,** *8* (24), 14966-14974.
10. Ivanova, E. P.; Hasan, J.; Webb, H. K.; Gervinskas, G.; Juodkazis, S.; Truong, V. K.; Wu, A. H.; Lamb, R. N.; Baulin, V. A.; Watson, G. S., Bactericidal activity of black silicon. *Nature communications* **2013,** *4* (1), 1-7.
11. Dickson, M. N.; Liang, E. I.; Rodriguez, L. A.; Vollereaux, N.; Yee, A. F., Nanopatterned polymer surfaces with bactericidal properties. *Biointerphases* **2015,** *10* (2), 021010.
12. Bhadra, C. M.; Truong, V. K.; Pham, V. T.; Al Kobaisi, M.; Seniutinas, G.; Wang, J. Y.; Juodkazis, S.; Crawford, R. J.; Ivanova, E. P., Antibacterial titanium nano-patterned arrays inspired by dragonfly wings. *Scientific reports* **2015,** *5* (1), 1-12.
13. Wang, X.; Bhadra, C. M.; Dang, T. H. Y.; Buividas, R.; Wang, J.; Crawford, R. J.; Ivanova, E. P.; Juodkazis, S., A bactericidal microfluidic device constructed using nano-textured black silicon. *RSC advances* **2016,** *6* (31), 26300-26306.

14. Van Doremalen, N.; Bushmaker, T.; Morris, D. H.; Holbrook, M. G.; Gamble, A.; Williamson, B. N.; Tamin, A.; Harcourt, J. L.; Thornburg, N. J.; Gerber, S. I., Aerosol and surface stability of SARS-CoV-2 as compared with SARS-CoV-1. *New England Journal of Medicine* **2020,** *382* (16), 1564-1567.
15. Walker, J., *Decontamination in Hospitals and Healthcare*. Woodhead Publishing: 2019.
16. Kramer, A.; Schwebke, I.; Kampf, G., How long do nosocomial pathogens persist on inanimate surfaces? A systematic review. *BMC infectious diseases* **2006,** *6* (1), 130.
17. Hasan, J.; Jain, S.; Padmarajan, R.; Purighalla, S.; Sambandamurthy, V. K.; Chatterjee, K., Multi-scale surface topography to minimize adherence and viability of nosocomial drug-resistant bacteria. *Materials & design* **2018,** *140*, 332-344.
18. Hasan, J.; Xu, Y.; Yarlagadda, T.; Schuetz, M.; Spann, K.; Yarlagadda, P. K., Antiviral and antibacterial nanostructured surfaces with excellent mechanical properties for hospital applications. *ACS Biomaterials Science & Engineering* **2020**.
19. Hasan, J.; Pyke, A.; Nair, N.; Yarlagadda, T.; Will, G.; Spann, K.; Yarlagadda, P. K., Antiviral Nanostructured Surfaces Reduce the Viability of SARS-CoV-2. *ACS Biomaterials Science & Engineering* **2020**.
20. Shi, H.; Yu, M.; Liu, J.; Rong, G.; Du, R.; Wang, J.; Li, S., Effect of alkaline etching on microstructure and anticorrosion performance of anodic film on Al-Mg-Si alloy. *Corrosion Science* **2020,** *169*, 108642.
21. Canyook, R.; Seubsom, P.; Sang-ngean, J.; Trirujirapapong, T.; Taweesup, K., Influences of sealing solutions on anodized layer properties of 7075 aluminium alloy. *Materials Today: Proceedings* **2018,** *5* (3), 9483-9488.
22. Alkire, R. C.; Gogotsi, Y.; Simon, P., *Nanostructured materials in electrochemistry*. John Wiley & Sons: 2008.
23. Lee, W.; Park, S.-J., Porous anodic aluminum oxide: anodization and templated synthesis of functional nanostructures. *Chemical reviews* **2014,** *114* (15), 7487-7556.
24. Zhang, Z.; Liu, Q.; He, M.; Tang, F.; Ying, Z.; Xu, H.; Song, Y.; Zhu, J.; Zhu, X., Quantitative Analysis of Oxide Growth During Ti Galvanostatic Anodization. *Journal of The Electrochemical Society* **2020,** *167* (11), 113501.
25. Zhu, X.-F.; Song, Y.; Liu, L.; Wang, C.-Y.; Zheng, J.; Jia, H.-B.; Wang, X.-L., Electronic currents and the formation of nanopores in porous anodic alumina. *Nanotechnology* **2009,** *20* (47), 475303.
26. Naderizadeh, S.; Dante, S.; Picone, P.; Di Carlo, M.; Carzino, R.; Athanassiou, A.; Bayer, I. S., Bioresin-based superhydrophobic coatings with reduced bacterial adhesion. *Journal of Colloid and Interface Science* **2020,** *574*, 20-32.
27. Palza, H.; Nuñez, M.; Bastías, R.; Delgado, K., In situ antimicrobial behavior of materials with copper-based additives in a hospital environment. *International journal of antimicrobial agents* **2018,** *51* (6), 912-917.
28. Schmidt, M. In *Copper surfaces in the ICU reduced the relative risk of acquiring an infection while hospitalized*, BMC proceedings, BioMed Central: 2011; p O53.
29. Warnes, S. L.; Highmore, C. J.; Keevil, C. W., Horizontal transfer of antibiotic resistance genes on abiotic touch surfaces: implications for public health. *MBio* **2012,** *3* (6), e00489-12.
30. American Society for Testing and Materials, E. In *2180-07*, 2012; pp 2180-07.
31. Association, J. S., Antimicrobial products: test for antimicrobial activity and efficacy. *Japanese Industrial Standard 2000; JIS Z 2801* **2000**.
32. Wiegand, C.; Völpel, A.; Ewald, A.; Remesch, M.; Kuever, J.; Bauer, J.; Griesheim, S.; Hauser, C.; Thielmann, J.; Tonndorf-Martini, S., Critical physiological factors influencing the outcome of antimicrobial testing according to ISO 22196/JIS Z 2801. *PloS one* **2018,** *13* (3), e0194339.
33. Knobloch, J. K.-M.; Tofern, S.; Kunz, W.; Schütze, S.; Riecke, M.; Solbach, W.; Wuske, T., "Life-like" assessment of antimicrobial surfaces by a new touch transfer assay displays strong superiority of a copper alloy compared to silver containing surfaces. *Plos one* **2017,** *12* (11), e0187442.

34. Gross, T. M.; Lahiri, J.; Golas, A.; Luo, J.; Verrier, F.; Kurzejewski, J. L.; Baker, D. E.; Wang, J.; Novak, P. F.; Snyder, M. J., Copper-containing glass ceramic with high antimicrobial efficacy. *Nature communications* **2019,** *10* (1), 1979.
35. Pogodin, S.; Hasan, J.; Baulin, V. A.; Webb, H. K.; Truong, V. K.; Nguyen, T. H. P.; Boshkovikj, V.; Fluke, C. J.; Watson, G. S.; Watson, J. A., Biophysical model of bacterial cell interactions with nanopatterned cicada wing surfaces. *Biophysical journal* **2013,** *104* (4), 835-840.
36. Lin, N.; Berton, P.; Moraes, C.; Rogers, R. D.; Tufenkji, N., Nanodarts, nanoblades, and nanospikes: Mechano-bactericidal nanostructures and where to find them. *Advances in colloid and interface science* **2018,** *252*, 55-68.